A&A 531, A17 (2011)
DOI: 10.1051/0004-6361/201116984

Astronomy & Astrophysics

Quiet-Sun imaging asymmetries in Na I D_1 compared with other strong Fraunhofer lines

R. J. Rutten[1,2], J. Leenaarts[1], L. H. M. Rouppe van der Voort[2], A. G. de Wijn[3], M. Carlsson[2,4], and V. Hansteen[2,4]

[1] Sterrekundig Instituut, Utrecht University, Postbus 80 000, 3508 TA Utrecht, The Netherlands
e-mail: R.J.Rutten@uu.nl
[2] Institute of Theoretical Astrophysics, University of Oslo, PO Box 1029, Blindern, 0315 Oslo, Norway
[3] High Altitude Observatory, NCAR, PO Box 3000, Boulder, CO 80307–3000, USA
[4] Center of Mathematics for Applications, University of Oslo, PO Box 1053, Blindern, 0316 Oslo, Norway

Received 30 March 2011 / Accepted 21 April 2011

ABSTRACT

Imaging spectroscopy of the solar atmosphere using the Na I D_1 line yields marked asymmetry between the blue and red line wings: sampling a quiet-Sun area in the blue wing displays reversed granulation, whereas sampling in the red wing displays normal granulation. The Mg I b_2 line of comparable strength does not show this asymmetry, nor does the stronger Ca II 8542 Å line. We demonstrate the phenomenon with near-simultaneous spectral images in Na I D_1, Mg I b_2, and Ca II 8542 Å from the Swedish 1-m Solar Telescope. We then explain it with line-formation insights from classical 1D modeling and with a 3D magnetohydrodynamical simulation combined with NLTE spectral line synthesis that permits detailed comparison with the observations in a common format. The cause of the imaging asymmetry is the combination of correlations between intensity and Dopplershift modulation in granular overshoot and the sensitivity to these of the steep profile flanks of the Na I D_1 line. The Mg I b_2 line has similar core formation but much wider wings due to larger opacity buildup and damping in the photosphere. Both lines obtain marked core asymmetry from photospheric shocks in or near strong magnetic concentrations, less from higher-up internetwork shocks that produce similar asymmetry in the spatially averaged Ca II 8542 Å profile.

Key words. Sun: photosphere – Sun: chromosphere – Sun: surface magnetism – Sun: faculae, plages

1. Introduction

Three technological advances currently improve optical studies of the solar atmosphere. First, adaptive optics and numerical postprocessing deliver angular resolution in groundbased imaging well beyond the atmospheric Fried limit (rarely larger than 10 cm equivalent aperture even at the best sites). Second, multi-line imaging spectroscopy leaped forward with fast-tuning narrow-band Fabry-Pérot interferometers at the major solar telescopes. Third, numerical MHD simulations have evolved into productive analysis tools of small-scale near-surface magneto-convection and are becoming reliable emulators of fine structure higher up in the solar atmosphere.

In this paper we combine these advances in a comparative study of the formation of three of the strongest lines accessible to the current generation of Fabry-Pérot instruments, which all observe in the red part of the spectrum. The three lines are the b_2 line of Mg I at $\lambda = 5172.698$ Å (henceforth "Mg line"), the D_1 line of Na I at $\lambda = 5895.940$ Å (henceforth "Na line"), and the infrared-triplet line of Ca II at $\lambda = 8542.144$ Å (henceforth "Ca line"). The wavelengths are for standard air and taken from Moore et al. (1966).

These three lines are often taken to be diagnostics of the solar chromosphere, together with Hα which gave the chromosphere its name through its off-limb spectral dominance (Lockyer 1868; see Rutten 2010). On the solar disk Hα displays dense canopies of fibrils that cover active regions, network, and even quiet-Sun internetwork cell interiors except in the very quietest regions. The detailed comparison between Hα and the Ca line by Cauzzi et al. (2009) shows that the latter line displays these chromospheric fibrils similarly near quiet-Sun network but with smaller extent, whereas in quiet internetwork cell centers it samples the domain of generally cool but shockwave-ridden gas below the fibrilar canopies that was termed "clapotisphere" by Rutten (1995). We use this name here also, reserving "chromosphere" for the fibril canopies seen in Hα. The Na core is mostly formed within the wave-dominated clapotispheric domain, as shown by Leenaarts et al. (2010). We show below that the same holds for the Mg core.

The present study is a companion to the observational Hα – Ca line comparison of Cauzzi et al. (2009) by now comparing the Na and Mg lines to the Ca line. It is a direct extension of the observation–simulation comparisons by Leenaarts et al. (2009) for the Ca line and by Leenaarts et al. (2010) for the Na line, by now comparing these lines with another and with the Mg line. However, in this study the emphasis does not lie on the chromospheric or clapotispheric response of the cores of these lines but rather on their inner-wing formation in layers only 100–200 km kilometer above the surface, where the phenomenon of "reversed granulation" dominates the observed scene (e.g., Leighton et al. 1962; Evans 1964; Evans & Catalano 1972; Canfield & Mehltretter 1973; Altrock & Musman 1976; Nordlund 1984b; Suemoto et al. 1987, 1990; Rutten et al. 2004; Leenaarts & Wedemeyer-Böhm 2005; Janssen & Cauzzi 2006; Cheung et al. 2007). The topic of this paper is not its physical nature, but how how this domain appears in the three lines.

This study started with the data shown in Fig. 1 from the CRISP imaging spectrometer at the Swedish 1-m Solar

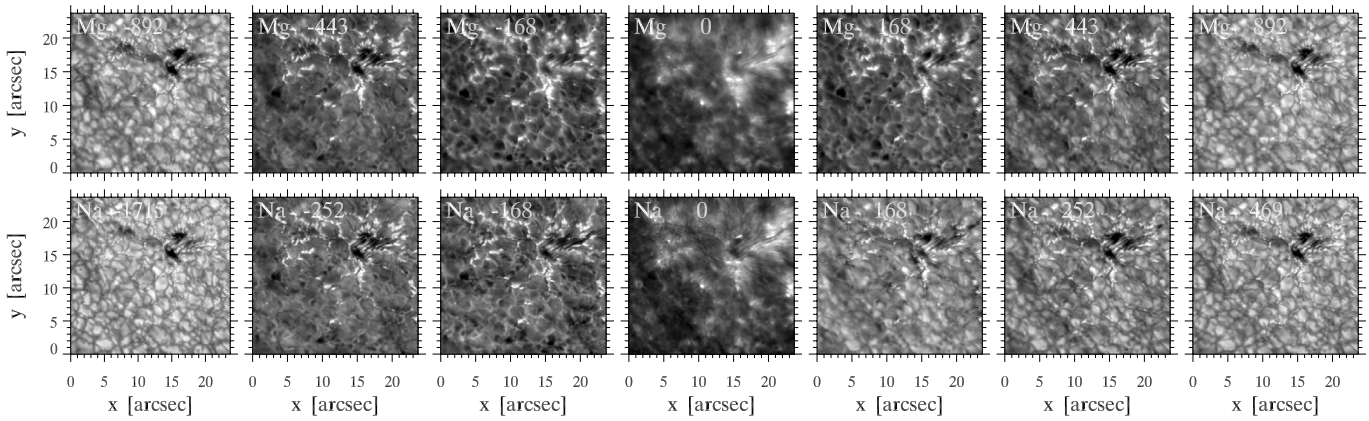

Fig. 1. Profile-sampling image comparisons between the Mg line (*upper row*) and the Na line (*lower row*). These images are subfield cutouts from a dual-line SST/CRISP profile scan taken on August 23, 2010. They sample a small active region with pores in the upper part and a quiet area in the lower part of the subfield. Each image is byte-scaled independently and is labeled with its wavelength separation $\Delta\lambda$ from line center in mÅ. Both sequences sample the line profile from the outer blue wing through the core to the outer red wing. The $\Delta\lambda$ values in the first two columns were selected for scene similarity between the two lines. The next two columns were also selected for scene similarity but have equal $\Delta\lambda$ values for the two lines. The final three columns mirror the $\Delta\lambda$ values of the first three. All images show rich detail; we invite the reader to magnify them with a pdf viewer. This paper explains the imaging asymmetry between the two lines in the red-wing panels where the Mg line shows reversed granulation as in its blue wing, whereas the Na line instead shows normal granulation as in the last panel.

Telescope (SST, La Palma). They sample the Mg and Na lines from a small active region. We first inspected the line-center images in the fourth column. They display bright fine-scale fibrilar structure near some pores, next to dark internetwork elsewhere. Thus, the Mg and Na cores do display some chromospheric response, i.e., can be opaque in fibrils. These line-center images are remarkably similar for the two lines.

We then compared the images taken in the blue wings of the two lines and quickly found that for every scene observed in the one line, a nearly identical scene can be found in the other. One only has to search further out into the much stronger Mg wing. We concluded that these wings sample the same solar layers similarly, and that there is no point in observing them both.

However, when we then turned to the red wings we were surprised by the striking difference illustrated in Fig. 1: in the red Na wing the reversed granulation drops out. The Mg line shows reversed granulation in its red wing that is similar to that in its blue wing, but in the Na red wing the line-center scene of chromospheric activity is quickly replaced by granulation, without an intermediate stage exhibiting reversed granulation. Along the red Na wing one seems to suddenly drop from chromospheric and clapotispheric sampling at line center to photospheric granulation sampling further out.

These inspections were made at the SST while T. D. Tarbell (LMSAL, Palo Alto) and P. Sütterlin (ISP, Stockholm) were present. The first commented that he had noted this reversed/non-reversed granulation asymmetry between the Na line wings in Hinode/SOT images and had wondered about its cause. The second suggested granular brightness-Dopplershift correlation as in Fig. 6 of Sütterlin et al. (2001).

Their suggestions were followed up in an observing campaign at the SST during October 2010, targeting truly quiet Sun to better view reversed granulation and adding the Ca line because it must sample the same scenes somewhere along its extended wings. We analyze the best resulting data here, comparing them to modeling predictions from a three-dimensional MHD simulation snapshot following Leenaarts et al. (2009, 2010).

Below, we describe the observations in Sect. 2, the simulation and the spectral synthesis in Sect. 3, and the results in Sect. 4. Since the latter consist of profile-sampling image cubes for the three lines for both observations and simulations, we use a common format permitting direct comparison to inspect the observed and simulated cubes in a parallel descriptive characterization of what they show. We then start the interpretation in Sect. 5 by reviewing what one expects from mean-profile inspection and from NLTE line synthesis with a standard one-dimensional hydrostatic solar-atmosphere model. We use these insights to interpret the results and explain most observed features. We add Hinode images as indicator of center-limb behavior, and end the paper with discussion in Sect. 7 and conclusions in Sect. 8.

2. Observations

2.1. SST/CRISP observations

The CRisp Imaging SpectroPolarimeter (CRISP, Scharmer et al. 2008) at the Swedish 1-m Solar Telescope (SST, Scharmer et al. 2003a) contains a dual Fabry-Pérot tunable filter system. It is designed for diffraction-limited narrow-band imaging with fast passband tuning sampling multiple spectral lines at rapid cadence in the wavelength range 5100–8600 Å.

The observing campaign, which was educationally oriented involving Oslo students on-site, suffered from bad observing conditions. However, on the last day, October 30, 2010, there was a 40-min period of moderate-quality seeing permitting observation of a region close to disk center (Stonyhurst heliographic coordinates (N4, W0) degrees) that was selected for its absence of any rosettes or other chromospheric activity in Hα.

The observing sequence sampled four spectral lines: the Mg, Na and Ca lines discussed here and also Fe I 6302 Å at $\Delta\lambda = -0.048$ Å from line center to obtain magnetograms. The Mg line was sampled at 41 wavelengths between $\Delta\lambda = \pm 0.892$ Å from line center with a passband with $FWHM = 32$ mÅ, the Na line at 41 wavelengths between $\Delta\lambda = \pm 1.715$ Å with passband 57 mÅ, the Ca line at 47 wavelengths spanning $\Delta\lambda = \pm 2.717$ Å with passband 111 mÅ. The sampling had regular spacing across each core but was sparser in the outer wings. The scan durations were about 10 s per line. At every wavelength step 8 exposures were

acquired. Since the cameras operated at 35 frames/s speed and the prefilter change time ranged from 0.27 s to 0.52 s, the total duration for one complete scan through all 4 lines was 29.7 s. We selected the best scan for this analysis. It was taken from 09:09:03 to 09:09:33 UT.

The spatial resolution of these observations was improved beyond the seeing Fried limit by using the SST adaptive optics system described by Scharmer et al. (2003b) and by subsequent postprocessing with the Multi-Object Multi-Frame Blind Deconvolution (MOMFBD) technique of van Noort et al. (2005). More details on such image reduction are given in, e.g., van Noort & Rouppe van der Voort (2008) and Rouppe van der Voort et al. (2009). The field of view after this processing and co-alignment is 58×56 arcsec^2, with 0.0592 arcsec/px or 42.6 km/px scale. However, the figures below show only a smaller area which equals the horizontal simulation extent.

2.2. Conversion to brightness temperature

The brightness temperature T_b is the formal temperature that yields $B_\lambda(T_\mathrm{b}) = I_\lambda^\mathrm{obs}$, i.e., that reproduces the observed intensity when entered into the Planck function. It equals the gas temperature T_gas at the height where $\tau_\lambda = 1$ along a radial line of sight when LTE and the Eddington-Barbier approximation are valid. LTE does not hold for the cores of our lines, but we nevertheless convert intensities into brightness temperatures to enable comparisons that are not affected by the differences in Planck function sensitivity to temperature at different wavelengths.

The inverse Planck operation requires rescaling of the observed intensities into absolute units. We did this by comparison to the solar disk-center spectrum atlas obtained by Brault and Testerman with the Fourier Transform Spectrometer (FTS) at Kitt Peak, calibrated by Neckel & Labs (1984) and spread by Neckel (1999). We smeared the atlas profiles of the three lines with the corresponding CRISP spectral transmission functions, i.e., the product of the measured prefilter transmission and the theoretical transmission of each of the two etalons at the line wavelengths. The resulting functions have a prominent symmetrical sidelobe pattern, with the first pair reaching 0.001 relative amplitude at $\Delta\lambda = \pm 2.2$ Å for the Na line. Convolving the atlas profiles with these makes the line cores rise substantially. For each line, we rescaled the data units of the spatially-averaged observed profile to the absolute intensities of the smeared atlas profile by determining their ratio for the wavelength with the highest outer-wing intensity in the observed profile. The observed and the smeared atlas cores show satisfactory agreement (last column of Fig. 9), confirming that the transmission functions give an adequate description of the spectral smearing.

2.3. Hinode observations

The Hinode satellite (Kosugi et al. 2007) was programmed to observe at several center-to-limb positions along the central meridian on December 4, 2010 between 14:14:33 and 15:33:41 UT using the Narrowband Filter Imager (NFI) fed by the 0.5 m Solar Optical Telescope (SOT, Tsuneta et al. 2008; Suematsu et al. 2008). Successive scans sampling the spectrum in 80 mÅ steps from −480 to +480 mÅ from line center were made through the Mg line and the Na line, with bandwidths 74 and 84 mÅ, respectively. One line scan took approximately 22 s. The prefilter changes and context images taken with the Broadband Filter Imager added 10 s delay between successive line scans. The data

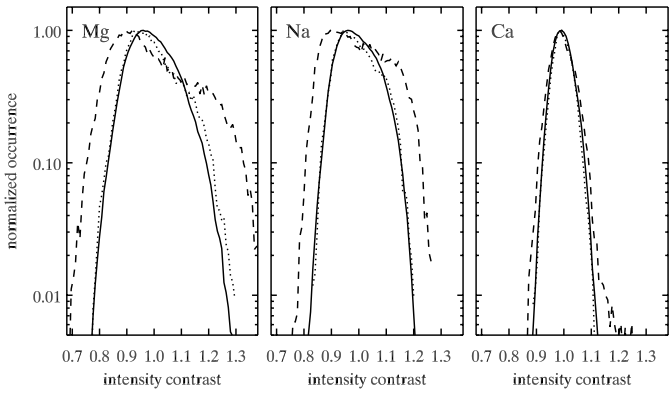

Fig. 2. Intensity contrast comparisons for the three lines between observations (solid), simulation (dashed), and the smeared simulation (dotted). Each curve shows the normalized occurrence distribution of pixels with the given contrast (intensity divided by the spatial mean) for the sum of the blue and red outermost-wing image pairs.

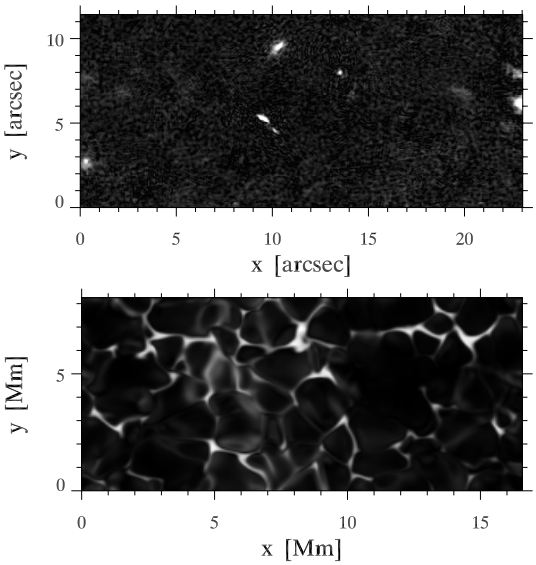

Fig. 3. Unsigned magnetic field distributions. *Top*: observed Stokes-V amplitude at $\Delta\lambda = -0.048$ Å in the Fe I 6302 Å line for the subfield. Only a few small magnetic concentrations have signal above the noise. The two major ones near $x = 10$ have opposite polarity. *Bottom*: field amplitude in the simulation at $h = 0$ km, corresponding to spatially-averaged $\tau_5 = 1$ in the continuum at $\lambda = 5000$ Å. The field is bipolar, as shown in Fig. 5 of Leenaarts et al. (2010). Throughout this paper image scales are in arcsec, simulation scales in Mm. The two areas have equal solar-surface extent.

were processed with the standard SolarSoft *fg_prep* pipeline. We selected small subfields of the size of the simulation extent from the pointings at $\mu = 1.0$, 0.5, and 0.35, where $\mu \equiv \cos\theta$ with θ the viewing angle, for display in Sect. 6.

3. Simulations

3.1. Simulation snapshot

We employ the same snapshot from a 3D radiation-MHD simulation performed with the Oslo Stagger Code (Hansteen et al. 2007) that was used in Leenaarts et al. (2009) for Ca line synthesis and in Leenaarts et al. (2010) for Na line synthesis. This simulation snapshot contains significantly more magnetic field than the observations (Fig. 3), but we prefer to re-use the snapshot and spectral line synthesis nevertheless because otherwise

we would have to re-do and re-display much analysis and diagnosis presented in Leenaarts et al. (2009, 2010) that we can now simply refer too.

The (x, y, z) snapshot grid measures $256\times128\times160$ sampling points, corresponding to a physical size of $16.6\times8.3\times15.5$ Mm^3 with the height ranging from the upper convection zone to the corona. The grid spacing is 65 km/px in the horizontal x and y directions; in the vertical z direction it varies from 32 km at the bottom to 440 km at the top. The snapshot contains bipolar magnetism with a mean field strength of 150 Gauss in the photosphere. The vertical field magnitude at the bottom of the photosphere is shown in Fig. 3. Figure 5 of Leenaarts et al. (2010) displays various physical quantities, including field strength, at different heights in the simulation.

3.2. Radiative transfer

For the Ca line and the Na line we also re-use the line synthesis described in Leenaarts et al. (2009, 2010), respectively, to which we refer for further detail. These radiative transfer computations were performed in 3D geometry using the code Multi3D of Botnen (1997) and Leenaarts & Carlsson (2009) which is based on the 1D code MULTI of Carlsson (1986). For this paper, simpler profile synthesis of the Mg line was added by using MULTI and assuming each vertical column of the simulation snapshot to describe the stratifications of a plane-parallel 1D atmosphere.

Because 3D radiative transfer computation is very computationally demanding, the model atom for Na described in Leenaarts et al. (2010) contains only the levels governing the line, the continuum, and an intermediate level with large collision bound-free coupling to ensure the "photon suction" population flow that tends to populate the Na I ground state (Bruls et al. 1992). The model atom for Ca was a simple 5-level plus continuum one which is adequate to describe the formation of Ca II H & K and the Ca II infrared triplet including our Ca line (e.g., Uitenbroek 1989). The model atom for Mg used here was a 13-level plus continuum model that was also used by Fleck et al. (2010) and is based on the 65-level plus continuum model atom of Carlsson et al. (1992). The level reduction used the method of Bard & Carlsson (2008). Photoionization was evaluated with line-blocking accounted for by opacity sampling in 9000 wavelength points as described by Collet et al. (2005).

3.3. Spectral and spatial smearing

In order to mimic the observations we first smeared the simulation intensities in the spectral domain with the CRISP transmission functions discussed in Sect. 2.2. Their effect is large in the line cores and small in the outer wings (Fig. 9).

Subsequently, we smeared the simulation spatially with an estimated SST point spread function (PSF). Its determination is less straightforward. Even the shape of the typical PSF remains in debate. Levy (1971) adopted the sum of two Gaussians, as did Deubner & Mattig (1975), but Nordlund (1984a) advocated the sum of two Lorentzians instead. Collados & Vázquez (1987) tested both formalisms and concluded that the choice strongly affects granulation contrast values that result from restoration by deconvolution. Schüssler et al. (2003) used the sum of the SST's theoretical Airy function and a Lorentzian to describe the atmospheric degradation, while the comparable paper by Shelyag et al. (2004) smeared the same simulation with the sum of the DOT's theoretical Airy function and a two-parameter wing function following Eq. (6) of Collados & Vázquez (1987), which is not a Lorentzian but describes the straylight across a knife-edge such as the lunar limb when the PSF is Lorentzian. Wedemeyer-Böhm (2008) and Wedemeyer-Böhm & Rouppe van der Voort (2009) defined PSFs for seeing-free imaging with Hinode/SOT as the convolution of the theoretical Airy function and a Voigt function, best-fitting the Voigt parameters with Mercury transit and eclipse data.

In our case both seeing and scattering cause angular smearing, we have no eclipse or transit data to measure their effects, and we must cope with the wavelength variation between our lines. We therefore do not aim to obtain a reliable PSF for data deconvolution, but simply apply somewhat realistic smearing to the simulation as illustration of its likely effect. We chose to use a single Voigt profile, representing the convolution of the Gaussian approximation to the Airy function $A(r) \approx 1/(\sqrt{2\pi}\,w)\,\exp(-r^2/2w^2)$ with extended Lorentzian tails $L(r) = \gamma/(4\,\pi^2)/[(\gamma/4\pi)^2+r^2]$ describing scattering, and assume circular symmetry with radius r as variable. In principle, the Airy width is $w = 0.42\,\lambda/D$, but since the seeing during this observation was only mediocre (in terms of the superb seeing that the La Palma site offers at its best), the MOMFBD restoration probably did not reach the full-aperture resolution. We therefore reduce the aperture D entering the Airy component to an "effective" one with a fractional factor f and scale the resulting $w \propto \lambda^{-1/5}$ as given by atmospheric turbulence theory (see Roddier 1981). The Voigt parameter $a = \gamma/(4\pi\sqrt{2}\,w)$ is scaled with λ^s. We thus have three fit parameters: f, a, and s.

As fit constraints we used the resulting contrast distribution and the visual appearance of the granulation at the extremes of our common wavelength ranges, i.e., the deepest-formed wavelengths that permit observation-simulation comparison. These differ per line. We use these extremes because the simulation is probably most realistic at the granulation level (indeed, most recent solar PSF estimates aim to show that granulation simulations are more reliable than PSF-challenged observations). We sum these outer wing images as a first-order compensation for Dopplershifts. (It would be better to use parallel nearby-continuum observations but the CRISP prefilters do not permit taking such.) We found that the combination of $f = 0.5$ and $a = 0.2$ at the wavelength of the Mg line with $s = -2$ produces both the acceptable contrast fits shown in Fig. 2 and similar appearance of the observed and smeared granulation (not shown, but compare the outer rows of Figs. 4 and 6). The value $f = 0.5$ seems realistic for non-superb seeing; $a = 0.2$ adds extended wings below the 1% level, and $s = -2$ describes scattering between the Rayleigh and Mie limits. The differences in distribution width between panels in Fig. 2 primarily reflect different Planck function sensitivities to temperature. The dip and enhanced righthand tail, most clearly present for the Mg line, are due to the appreciably larger amount of magnetism in the simulation.

4. Results

In this section we present displays from the profile-sampling image cubes for the three lines from the observations and from the simulation, likewise and in a common format. These figures serve to supply a comparative empirical inventory of what quiet-Sun fine structures the three lines display, in parallel for observation and simulation, while postponing all interpretation to Sect. 5. We again invite the reader to magnify the figures per pdf viewer for better appreciation of their detail.

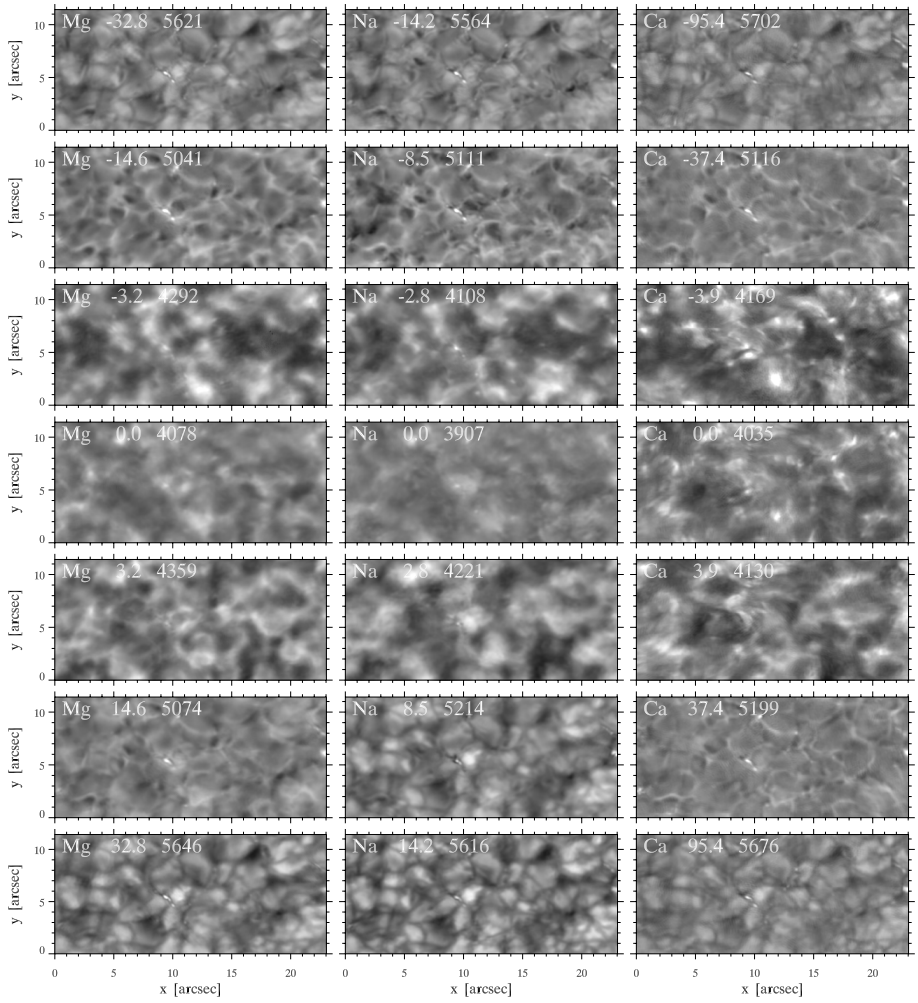

Fig. 4. Observed brightness-temperature images for selected wavelengths sampling the profiles of the Mg line (first column), Na line (second column), and Ca line (third column). The area is a small cutout of the center of the full field of view that corresponds in size to the horizontal extent of the numerical simulation. The identifier in each panel specifies the line, the CRISP passband offset from line center in km s^{-1} with redshift positive, and the mean brightness temperature over the full field of view. The grayscale range of each panel is clipped at $\Delta T_b = \pm 400$ K relative to this mean, so that each panel covers the same brightness temperature range in magnitude. The passband offsets select equal FALC formation height across the first and last two rows (optical depth unity near h = 65 and 150 km, respectively) and near-equal wavelength offset $\Delta\lambda$ from the nominal line center wavelength in Dopplershift units across the middle three rows (about $\Delta\lambda = -3$, 0, and +3 km s^{-1}, respectively). The selections are symmetrical with respect to line center (central row).

4.1. Magnetograms

Figure 3 compares the magnetic field in the subfield of the observations and in the simulation. The observed magnetogram indicates apparent longitudinal flux density, the simulation panel displays intrinsic vertical field strength. The observed subfield has only a few very small magnetic concentrations; there are some larger ones elsewhere in the full field of view. The field in the simulation is shown quantitatively in Fig. 5 of Leenaarts et al. (2010), displaying the polarity distribution in the first panel and the lateral expansion of the magnetic concentrations with height in subsequent panels. The larger white patches in the simulation panel represent kilogauss concentrations. The few observed white patches are likely to also represent kilogauss fields. There is much more strong field in the simulation than in the observation, but it is nevertheless a relatively weak-field simulation; the field does not upset granular convection as is the case in strong network or plage.

4.2. Profile-sampling images

Figure 4 shows a selection of the observed line-sampling images, cut down to a small subfield at the center of the SST field of view of which the 23.1 × 11.5 arcsec^2 area equals the horizontal simulation extent. All panels have dynamic range $\Delta T_b = \pm 400$ K around the mean value over the full field of view. The conversion into brightness temperature and the common greyscale range make all panels intercomparable. Similarly, the wavelength separations from line center $\Delta\lambda$ are specified in Dopplershift units (km s^{-1}) to supply wavelength-independent comparison.

The $\Delta\lambda$ selections are specified in each panel and are symmetric along the columns around the line-center panels in the central row. They have been carefully selected to obtain similar atmospheric sampling in the three lines. For the first and second rows (and reversely the last and next-to-last rows) the $\Delta\lambda$ values are those that produce equal $\tau_\lambda = 1$ formation height in the FALC modeling described in Sect. 5.2 below, at $h = 65$ km and $h = 150$ km, respectively. The first height is the lowest at which we can do such three-line comparison, being limited by the outermost CRISP tunings in the extended wings of the Ca line. This height samples the top of the normal granulation. The second height was selected to sample reversed granulation. At both heights LTE is a good assumption (Sect. 5.2); indeed, the mean T_b values specified in each panel are similar along these rows and between opposite-wing pairs. Closer to line center we instead selected similar $\Delta\lambda$ values along rows, since these images may primarily sample clapotispheric structures in this very quiet area. Cloud-like line formation with specific cloud Doppler velocities should then produce similar scenes for lines with similar cloud opacities and source function variations.

The granulation appears closely similar along the first row, but not so along the bottom row where the Na line displays the largest granulation contrast, the Ca line the smallest. The reversed granulation also appears closely similar in all three lines along the second row, but not so in the next-to-last row where

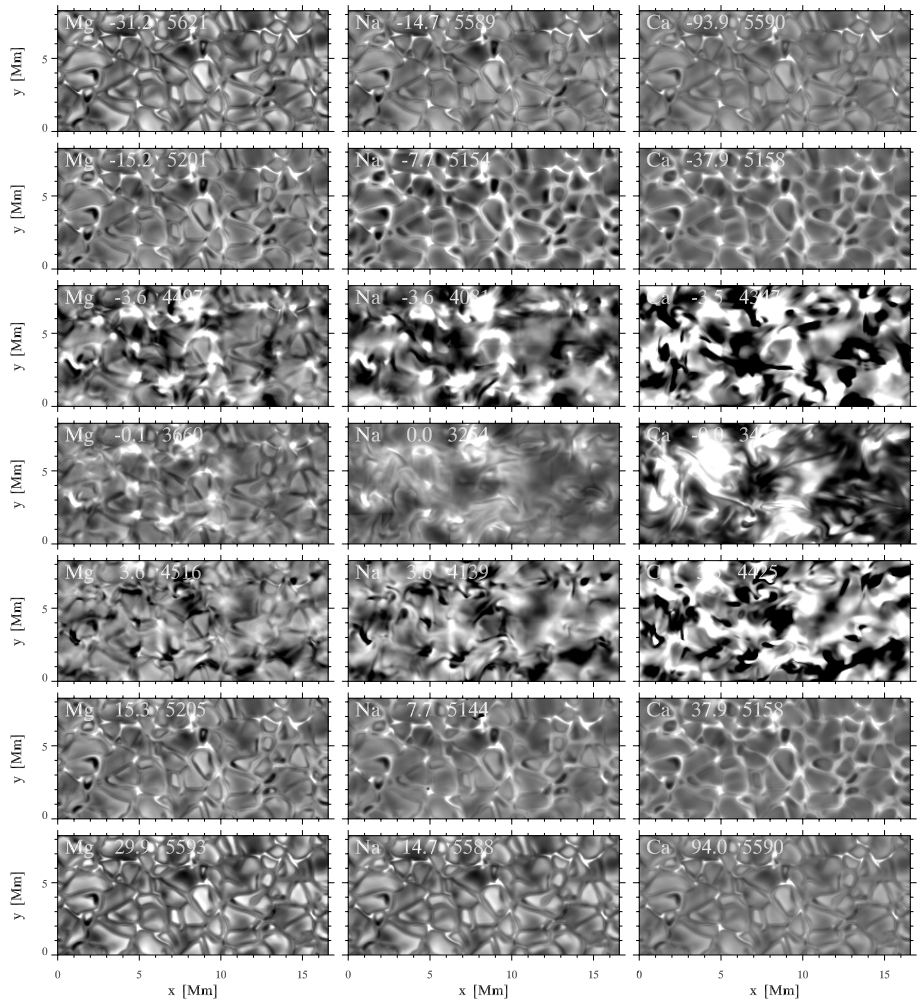

Fig. 5. Simulated brightness-temperature images for selected monochromatic wavelengths sampling the profiles of the Mg line (first column), Na line (second column), and Ca line (third column). The area equals the observed subfield in Fig. 4 in size. The format, labels and grayscales correspond to those of Fig. 4, i.e., each panel is again clipped at $\Delta T_b = \pm 400$ K relative to the spatially averaged mean. The wavelength selection, again specified in Dopplershift units, corresponds to the selection in Fig. 4, i.e., near-equal FALC formation height of about 65 km and 150 km along the outer rows and near-equal wavelength offset $\Delta\lambda$ from the nominal line center in Dopplershift units across the middle three rows, of which the center one samples nominal line center.

the Na line roughly shows the same granulation as in the bottom panel, whereas the Ca line displays the closest similarity to its blue-wing counterpart in the second row. These differences confirm the imaging asymmetries in Fig. 1.

The line core scenes in the central three rows are similar for the Mg and Na lines, but differ for the Ca line. For all three lines they differ much on the opposite sides of line center, with opposite grayscale patterns especially for Mg and Na. These patterns are patchy in morphology and appear fuzziest in the Na line. In the Ca line small roundish bright features appear, clearest on the blue side but not on the red side.

The few magnetic concentrations in this very quiet area (Fig. 3) appear as bright points, clearest in the second row (all three lines) and next-to-last row (Mg and Ca).

Figure 5 presents the companion display from the simulation. The $\Delta\lambda$ selections are the closest available to those in Fig. 4. In all panels the fine structure has appreciably larger brightness-temperature contrast than in Fig. 4, particularly in the central three line-core rows. The granulation has largest contrast along the top and bottom rows in the Mg line, smallest in the Ca line. The reversed granulation is most clear for Na in the second row, least clear for Na in the next-to-last row. In the latter it appears present as well, but all the bright patches and lanes in this panel represent strong magnetic field (compare with Fig. 3 and the bottom Na panel).

In the three line-core rows of Fig. 5 the Mg line displays dark intergranular lanes in all three rows, most strikingly at $\Delta\lambda = +3.6$ km s^{-1}. They are covered by higher-lying structures in the other two lines. These are grayish with much fine structure at Na line center but become black-and-white clipped at the 400 K display limits at Ca line center. They break up into smaller patches in the near-center panels, many opposite in black or white at the two sides.

Figure 6 repeats Fig. 5 after smearing. The simulation pixels (65 km) are actually coarser than the SST pixels (42.6 km on the observing date), but comparison of Figs. 4 and 5 suggests that the actual resolution of the observations is considerably worse. We therefore apply spectral smearing with CRISP's transmission profiles and spatial smearing with the estimated PSFs from Sect. 3.3 to illustrate their effect. The central three rows of Fig. 6 are most affected, especially with respect to the extended patches in the Na line. At line center, these loose the fine structure seen in Fig. 5 and become smoother greyish patches, appreciably darker than the bright magnetic concentrations and with similar appearance as the extended patches in the corresponding panel of Fig. 4. Dark intergranular lanes remain visible in the Mg core. The Na-line imaging asymmetry of reversed granulation in the second and next-to-last rows remains, but without showing dark lanes outside the field-filled ones in the red wing as observed in Fig. 4.

4.3. Dopplergrams

The various asymmetries above between the blue and red line wings obviously suggest a role of Dopplershifts. Therefore, Fig. 7 shows Dopplergrams, in the upper half for the

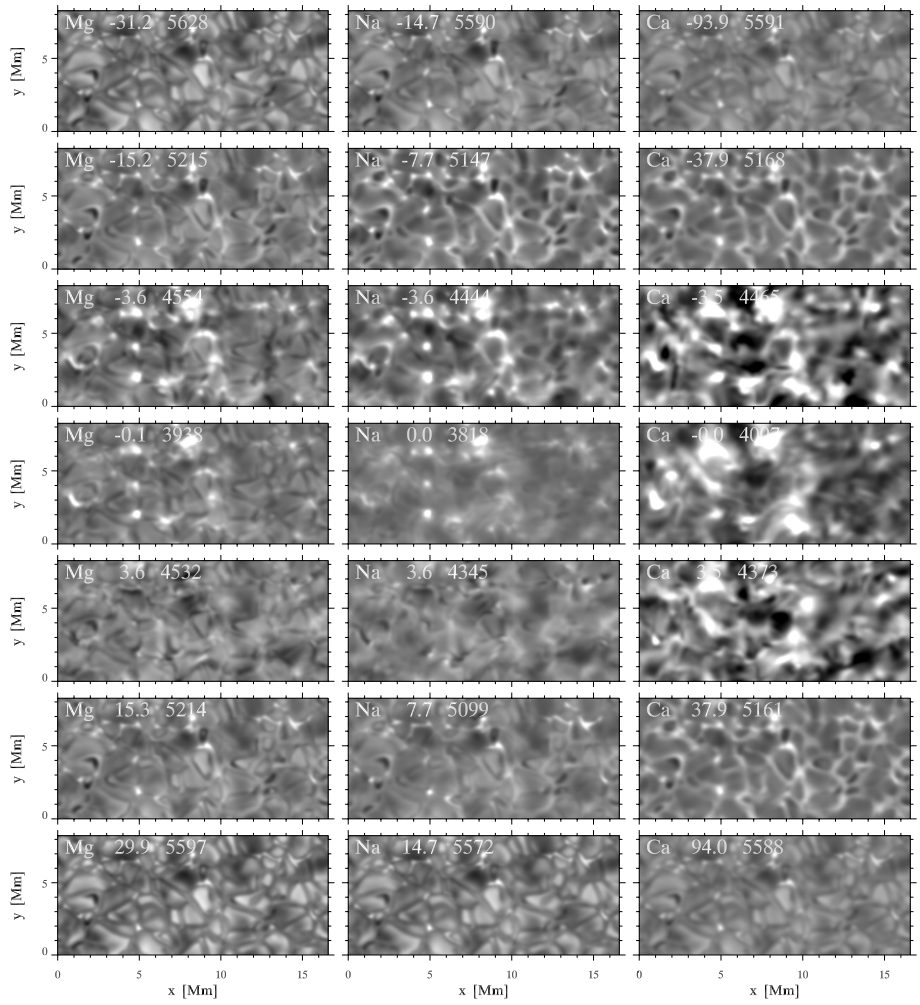

Fig. 6. The same simulated brightness-temperature images as in Fig. 5 but after spectral smearing with the CRISP transmission profiles described in Sect. 2.2 and spatial smearing with the point spread function estimates obtained in Sect. 3.3.

observations and in the lower half for the smeared simulation. The sign of the Dopplergram definition $D \equiv (T_b^{red} - T_b^{blue})/(T_b^{red} + T_b^{blue})$ is chosen to make the granular Dopplershift pattern appear as granulation, i.e., with bright granular updrafts and dark intergranular downdrafts. The D ranges are optimized per panel, but $D = 0$ is the same dark gray in each panel. The $\Delta\lambda$ selections correspond to those in Figs. 4–6. The first rows again sample the top of the normal granulation, the second rows the reversed granulation, the third rows the inner line cores.

In the observed Dopplergrams the pattern quality along the first row shows that the Na line has the best granular Doppler sensitivity, Ca the worst. Most structure in the Ca Dopplergram is noise or MOMFBD artifact that is much exaggerated by the greyscale optimization. In the Mg and Na panels some granules have larger positive (bright) Dopplershift than others. The reversed granulation sampled in the second row shows the same updraft pattern as the granulation in the first row, but the downdraft lane pattern is less clear than the updraft granule pattern.

The observed Mg and Na Dopplergrams in the third row have essentially three shades. The bright and dark patches (apart from the magnetic concentrations which appear as small black grains) correspond roughly to the areas with bright and less bright granules in the upper rows, respectively. The intermediate dark-gray background consists of unsharp granules (more clearly when we flip rapidly through adjacent Dopplergrams on our screen). These are not seen in the Ca core Dopplergram, in which the patches also have different patterning as well as finer texture. In this Dopplergram black grains appear also away from the magnetic concentrations. The strong updraft in the granule near the center of the field is visible as a roundish bright patch in the Mg and Na cores but not in the Ca core.

The simulation Dopplergrams also show the granulation pattern as dominant in the first row, a much fuzzier granulation pattern with the lanes washed out in the second row, and larger-scale patch patterns in the third row. The fine texture in the latter is similar for the Mg and Na lines, less so for the Ca line. The dark gray shade again corresponds to underlying granules in Mg and Na but not in Ca. They are less distinct than in the Mg-core brightness images in Fig. 6.

When we scan through all observed Dopplergrams, bright updraft patches appear first at $\Delta\lambda \approx 8$, 6, 15 km s^{-1} for the Mg, Na, Ca lines, respectively. Towards the line centers they become more opaque. In the simulations they appear only at $\Delta\lambda \approx 4$, 5, 5 km s^{-1}, respectively. The simulation Ca Dopplergrams show a very flat gray, nearly granule-free low-Dopplershift intermediate scene over $\Delta\lambda = 11$–6 km s^{-1} that is not sampled in the observations.

The more numerous magnetic concentrations in the simulation also stand out as black blobs in the lower Mg and Na panels. The dark patches in the Ca Dopplergram in the last panel have some but less good correspondence to the strongest fields.

4.4. Core asymmetries

The scatter diagrams in Fig. 8 demonstrate the field-Dopplershift correlations in more detail. They plot the core asymmetry ratio

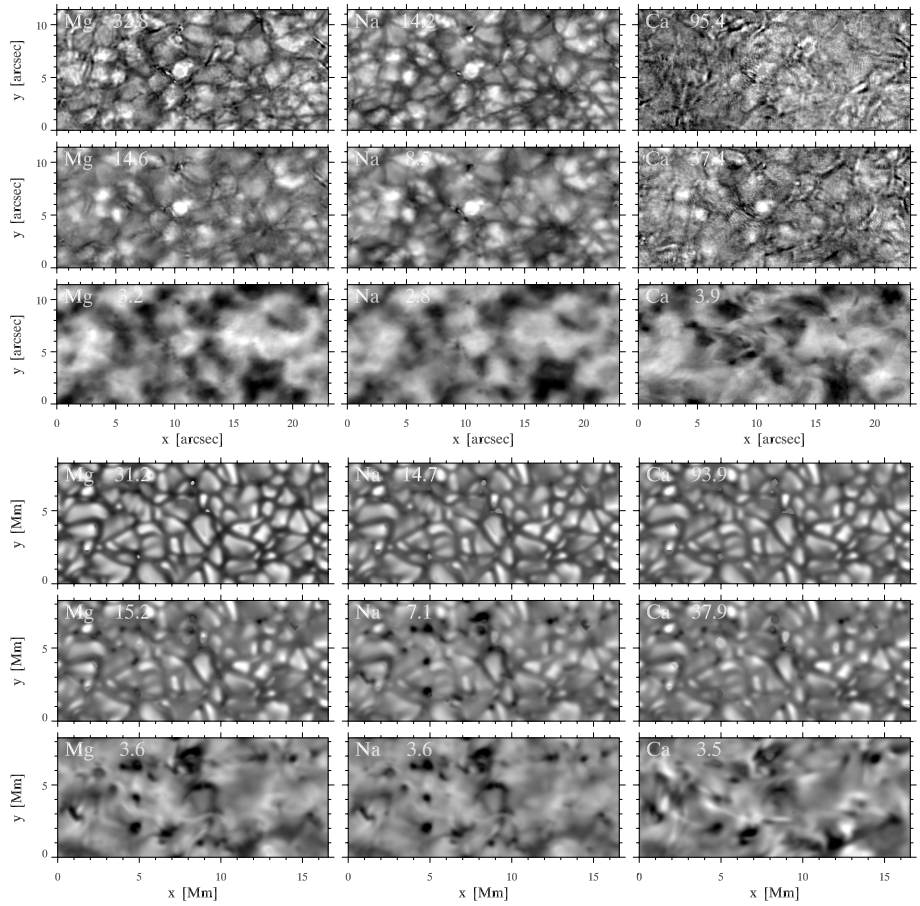

Fig. 7. *Upper assembly*: observed brightness-temperature Dopplergrams for the three lines in the format of Fig. 4. Each panel displays the normalized Dopplergram subtraction $D \equiv (T_b^{red} - T_b^{blue})/(T_b^{red} + T_b^{blue})$, with bright implying blueshift (updraft) for spectral absorption features and redshift (downdraft) for spectral emission features. The grayscale is defined so that $D = 0$ is represented by the same gray in all panels while the ranges are adapted per panel for largest contrast. The separations from line center $\Delta\lambda$, specified in km s^{-1} in each panel, are the same as in Fig. 4. *Lower assembly*: corresponding results from the smeared simulation. The $\Delta\lambda$ values are the same as in Figs. 5 and 6.

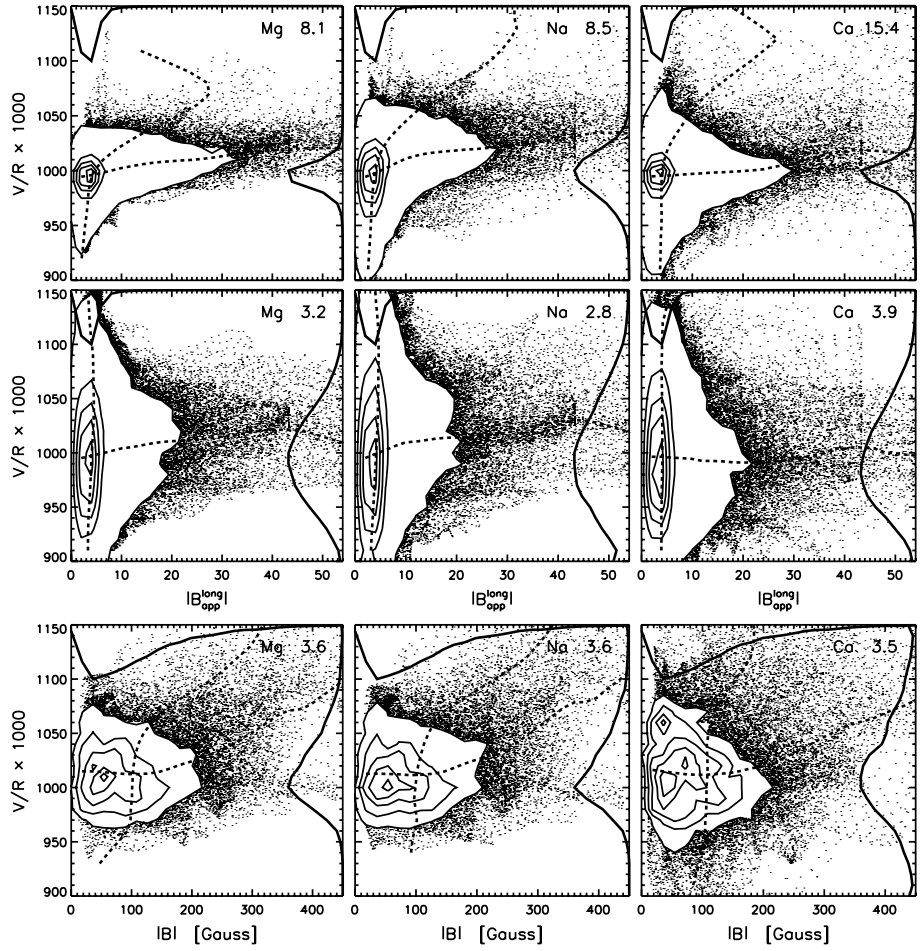

Fig. 8. Scatter diagrams of the core asymmetry ratio $V/R \equiv T_b^{blue}/T_b^{red}$ against field strength. *Upper two rows*: observations, using the full field of view. The abscissa is the magnitude of the apparent longitudinal flux density measured from the Fe I 6302 Å magnetogram, in arbitrary units and after 9-pixel spatial smoothing to mimic field spreading with height. *Bottom row*: smeared simulation. The abscissa is the magnitude of the vector field at height $z = 500$ km. *Left*: Mg line. *Center*: Na line. *Right*: Ca line. The sampling wavelength in km s^{-1} is specified in each panel. The V/R values are multiplied by 1000 for plotting reasons. Density contours replace individual pixels to avoid plot saturation. The solid curves are the distributions over V/R and field strength, respectively. The dashed curves show the first moments per bin per axis. They line up for high correlation and are perpendicular at no correlation.

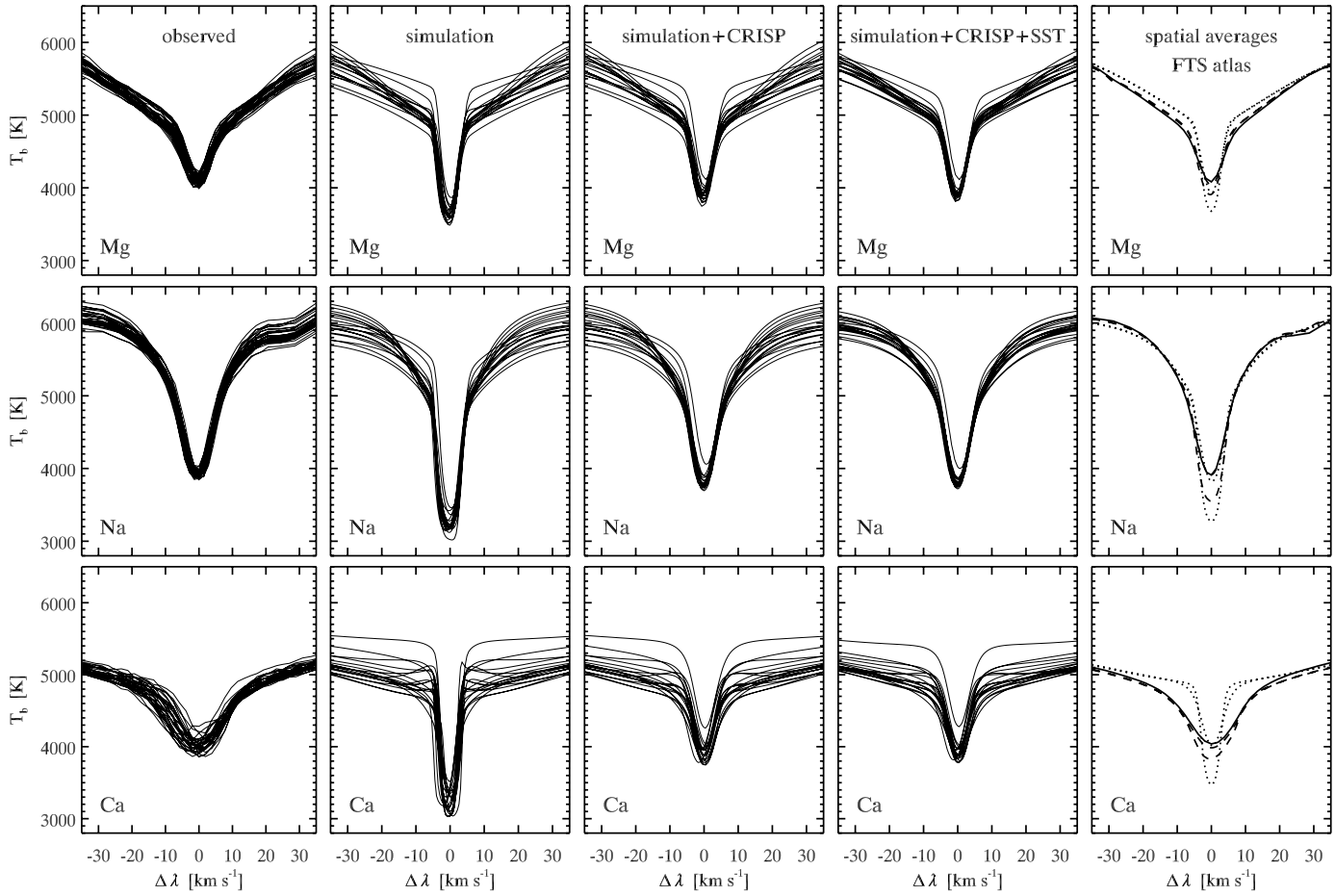

Fig. 9. Sample profiles of the cores of the Mg line (*top row*), Na line (*second row*), and Ca line (*third row*), for every 50th pixel in x and y in Figs. 4 and 5, respectively. *First column*: observed profiles. *Second column*: original synthetic profiles from the simulation. *Third column*: synthetic profiles spectrally smeared with the CRISP transmission profile. *Fourth column*: additional smearing with the estimated SST point spread function. The smearing was applied to the computed intensities, not the brightness temperatures. *Final column*: mean profiles. The solid curves are the observed full-field means, the dotted curves the simulation means without smearing and with CRISP and SST smearing (the latter does not affect the spatial mean). The dashed curves are the FTS atlas profiles without and with CRISP smearing. All panels cover the same coordinate ranges.

$V/R \equiv T_b^{blue}/T_b^{red}$ against field strength per pixel, both for the observations and for the simulation. (We use symbol V for "violet" to correspond to the Ca II H & K practice of e.g., Cram & Damé 1983, and to avoid confusion with the B for magnetic field). The sampling wavelengths for Mg and Na in the first and bottom rows are those that show the tightest high-high correlations (line-up of the two moment curves). These lie further out in the observed profiles than in the synthetic profiles. The observed Mg and Na diagrams in the first row show significant correlation between large V/R and large field strength. The observed Ca line shows similar correlation at double $\Delta\lambda$ from line center. The diagrams in the center row show that the high-high correlations remain similar close to line center (tilt of the horizontal first-moment curve), but many more weak-field pixels now contribute larger V/R. For all three lines the low-field mountain spreads out in V/R, with an extended distribution tail for the Na and Ca lines.

The scatter diagrams from the simulation (bottom row of Fig. 8) have very different field distributions corresponding to Fig. 3. They show similar correlations as the observations in the top row, but only close to line center. The V/R spreading and distribution tails are more like the observed ones near line center (center row).

4.5. Line profiles

Figure 9 concludes our parallel inspection of observation and simulation results. It shows random samples of observed line profiles in the first column, random samples of the simulated line profiles in the next three columns, and spatially averaged observed and simulated profiles together with FTS-atlas profiles in the last column. The spread between the sample profiles is much larger for the simulation than for the observation, but becomes similar with the CRISP and SST smearing. The simulated cores rise considerably with the CRISP smearing but do not become as shallow as the observed ones. The largest discrepancy is obvious in all simulation panels, and also in the last column: even after the CRISP smearing, the simulated line cores are narrower than the observed ones, not much for the Na line but markedly for the Ca line. This difference matches the differences in core-structure onset with $\Delta\lambda$ and core asymmetry sampling noted above.

5. Interpretation

5.1. Solar atlas profiles

We start with a comparison of the spatially-averaged profiles of the three lines. Figure 10 combines them with Hα in a

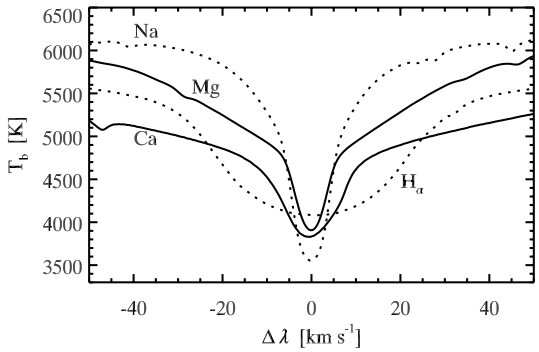

Fig. 10. Strong lines in the red part of the solar spectrum. Disk-center profiles of the Na line (Na I 5895.940 Å; dotted), the Mg line (Mg I 5172.698 Å), the Ca line (Ca II 8542.144 Å) and Hα (H I 6562.808 Å, dotted) from the FTS atlas are shown on common scales. The atlas calibration by Neckel & Labs (1984) was used to convert the intensities into formal brightness temperatures. The wavelengths were converted into formal Dopplershifts from line center, with redshift positive.

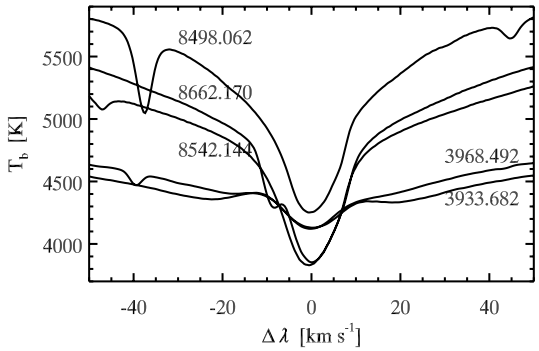

Fig. 11. Disk-center profiles of the five strongest Ca II lines from the FTS atlas. Format as for Fig. 10.

common-scale display of their profiles in the FTS atlas. The Na line is the deepest, so simple LTE modeling with a radiative-equilibrium model (as remains common practice in stellar spectroscopy) would declare this the highest-reaching one, sampling the coolest upper-atmosphere layers. However, at the same time it is the weakest in terms of equivalent width. The tabulation of Moore et al. (1966) gives only 564 mÅ for the Na line, compared to 1259 mÅ for the Mg line and 3670 mÅ for the Ca line. The spread of damping wings also suggests that the Mg line is stronger than the Na line, even though its core reaches less deep.

Hα (equivalent width 4020 mÅ) is shown for comparison. Its core is much wider than the others and even shallower than the Mg line. The large core width comes from large thermal broadening at the small hydrogen mass, making it a good temperature diagnostic (Cauzzi et al. 2009).

The cores of the Na and Mg lines appear similar apart from the larger Na line depth and the deeper onset of damping wings in the Mg line. The Ca core is markedly wider and displays marked asymmetry, whereas the other lines show good symmetry. That this is not due to blending is shown by Fig. 11 which combines the five strongest solar Ca II lines in the same comparison-enabling format. All five display similar red-blue core asymmetry. For H & K it appears as the K_{2V}/K_{2R} asymmetry between the slight emission features that set H & K apart from all other Fraunhofer lines in the visible as being the only ones not showing a simple absorption bell shape. The H & K asymmetries in spatially-averaged profiles are mostly due to H_{2V} and

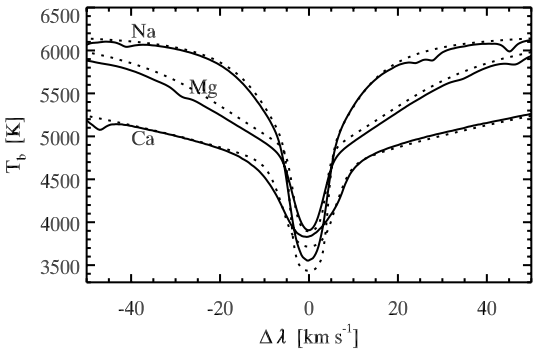

Fig. 12. Solid: the three lines in the FTS atlas, as in Fig. 10. Dotted: emergent line profiles for the FALC model in the same units.

K_{2V} internetwork grains (cf. review by Rutten & Uitenbroek 1991). These have been explained by Carlsson & Stein (1994, 1997) as acoustic shock interference, taking place in quiet-Sun clapotispheric gas below the fibrilar Hα chromosphere (cf. Rutten 1995). Similar but field-guided shocks in near-network dynamic fibrils (Hansteen et al. 2006; De Pontieu et al. 2007) may contribute similar asymmetry to the atlas profiles. Figure 11 suggests that the Ca II infrared triplet lines gain their asymmetry likewise. We return to this issue in Sect. 5.5 and conclude from this section that:

- the Mg and Na lines have similar cores but different wings;
- the imaging asymmetries in Fig. 1 are not accompanied by obvious Mg or Na mean-profile asymmetries;
- only the Ca line displays marked mean-profile asymmetry, which it shares with the other strong Ca II lines and therefore may be due to clapotispheric shocks above the photosphere.

5.2. Formation in the FALC atmosphere

After LTE Eddington-Barbier interpretation, the next stage in solar spectrum modeling is to relax the assumption of LTE but maintain the assumption of hydrostatic equilibrium in a plane-parallel simplification. Figure 12 shows results from such standard NLTE modeling using the standard FALC model of Fontenla et al. (1993) together with our model atoms in the MULTI spectral synthesis code. The FTS atlas profiles of the three lines are added for comparison. The pertinent photospheric and low-chromosphere parts of FALC are identical to those of the quiet-Sun models of Avrett (1985) and Maltby et al. (1986) and represent an update of the canonical VAL3C model of Vernazza et al. (1981). They were defined to fit solar continua, not these particular lines, but Fig. 12 shows that they do a rather good job for these as well. Our NLTE FALC modeling therefore serves well to discuss basic formation aspects of our lines.

Figure 13 diagnoses the FALC formation of the three lines by plotting various line formation parameters against height. The first panel plots population departure coefficients $b \equiv n/n_{\rm LTE}$ where n is the computed population and $n_{\rm LTE}$ the population that would follow from the Saha and Boltzmann equations from the abundance, gas temperature and electron density. They demonstrate that LTE holds to within 20% in the first few hundred kilometers of the photosphere. Above the FALC temperature minimum (shown by the $T_{\rm gas}$ curve in the center panel) the lower-level curves show steep increases with height that mark NLTE underionization in pertinent ionization edges. In these the ionization is dominated by photospheric radiation from below without following the FALC chromospheric temperature rise.

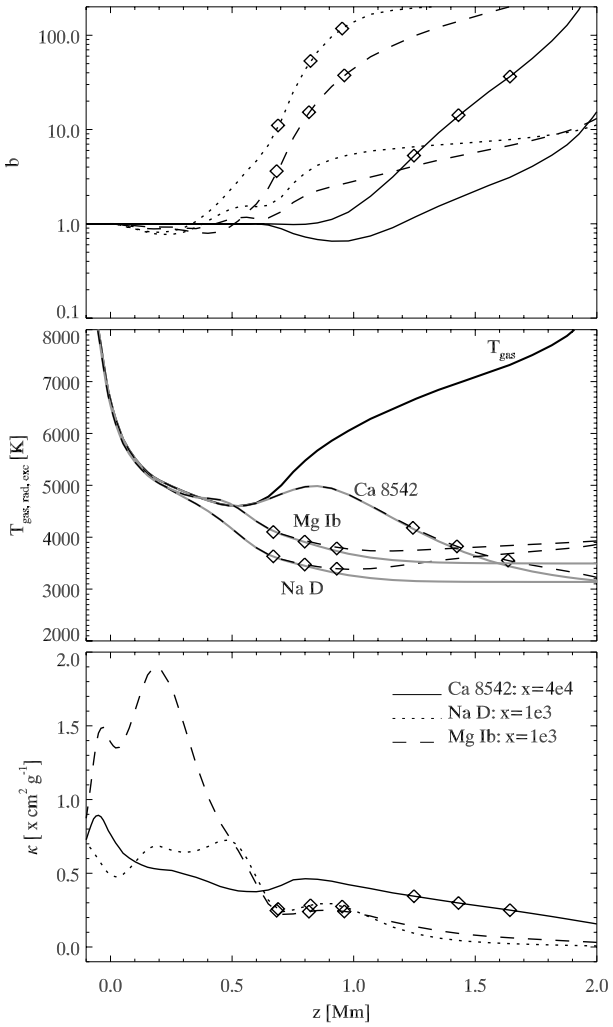

Fig. 13. Formation parameters of the three lines in the standard 1D model atmosphere of Fontenla et al. (1993) against geometrical height. The symbols mark the heights where the total optical depth at line center reaches 0.3, 1 and 3, respectively. *Top panel*: NLTE population departure coefficients b for the Mg line (dashed), Na line (dotted) and Ca line (solid). The optical depth marks are superimposed on the lower-level curves. *Middle panel*: total (opacity-weighted line plus continuum) source function in the form of a formal temperature $T_{\rm exc}$ (dashed) and mean radiation field in the form of a formal temperature $T_{\rm rad}$ (solid) for each of the three lines. The gas temperature $T_{\rm gas}$ is added for comparison. *Bottom panel*: scaled height variation of the total (line plus continuum) opacity per gram κ at the center of each line. The curve coding is the same as in the top panel. Note the compressed scale for the Ca line; its peak at $z = 0$ is 24 times the corresponding peak for the Mg line.

Ca II photo-ionization produces Ca lower-level overpopulation only at larger height.

Deeper down radiative overionization causes small lower-level Mg I and Na I underpopulation dips in the upper photosphere[1]. They are less deep than most atomic species had in the VAL3C model (e.g., Fe I in Rutten 1988) for two reasons. First, the FALC upper photosphere has a less steep temperature decline, and second, for these levels such dips are filled in by photon suction, as shown by Bruls et al. (1992) for Na I. This process of line-driven recombination also operates in Mg I and causes the Mg I 12-micron emission features (Carlsson et al. 1992). It produces the early onsets of the overpopulation rises in Fig. 13, earliest for the Na line.

For each line the upper-level departure coefficient (lower curve of each pair in the top panel) drops significantly below the lower-level one through resonance scattering. The dominance of scattering is obvious from the center panel in which the three source functions are close to the angle-averaged radiation field (in $T_{\rm exc}$ and $T_{\rm rad}$ incarnations to remove Planck function sensitivity differences). Since $S^l \approx (b_u/b_l)\, B$ (in the Wien limit), the divergences between the lower- and upper-level curves in the top panel define the divergences between the $T_{\rm gas}$ and $T_{\rm exc}$ curves in the center panel. Uitenbroek & Bruls (1992) have shown that the textbook case of two-level scattering is an excellent approximation for the Na line which is a resonance line. The others are not and may have larger multi-level coupling to the temperature, for the Ca line via H & K (see Owocki & Auer 1980; Uitenbroek 1989).

The Na source function drops deepest because it uncouples earliest from the Planck function and feels the FALC chromospheric temperature rise least. The Ca source function retains a hump from this rise and would display small inner-wing emission features in FALC modeling if the latter wouldn't apply the considerable VAL3C microturbulence.

The NLTE source functions and τ scaling explain the computed FALC line profiles in Fig. 12. Application of the Eddington-Barbier approximation to the $\tau = 1$ marks in the center panel recovers the computed line depths.

The bottom panel of Fig. 13 shows the buildup of the τ scales, which differs between the three lines (note the scale factors needed to overplot these curves within one panel). Plotting the opacity per gram takes out the density dependence. The curve patterns are the product of the Saha and Boltzmann population formulas, the shape of the line extinction profile, and the lower-level population departures b_l in the top panel.

Let us first discuss the κ curve for the Na line (dotted). The lower-level population/density ratio n_l/ρ of the Na line in LTE is set by the ionization equilibrium since this line is from the ground state and has no Boltzmann excitation sensitivity to temperature. This ratio (not shown) has an initial rise due to decreasing ionization in the initially steeply declining temperature, followed by a long decline due to larger ionization at lower electron density. The photospheric wiggle pattern in the actual Na-line κ curve is added by the b_l variations in the top panel and by changes in the line profile shape. The steep b_l rise halts the ionization decay near $z = 0.7$ Mm.

The Mg line has three times larger opacity in the lower photosphere but a much larger drop across the upper photosphere due to the sensitivity of its Boltzmann excitation to the declining temperature. The Na and Mg FALC opacities are nearly identical above $h = 0.5$ Mm.

The Ca line is from the dominant calcium ionization stage; ionization of Ca II to Ca III affects $\kappa_{\rm Ca}$ from $z = 0.9$ Mm. In the photosphere this line has no ionization sensitivity, only excitation sensitivity to the declining temperature. This sensitivity is smaller than for the Mg line (1.7 eV versus 2.7 eV excitation energy).

The wiggles in the deepest layers are set by the steep outward decrease of the electron/gas density ratio due to hydrogen recombination. It affects the ionization and also the balance

[1] More recently, Fontenla et al. (2009) claimed that the much deeper upper-photosphere b dips for Si II and the other electron-donor species in their newer models are due to irradiation from above, not from below, but this is a misinterpretation due to using the Menzel definition for departure coefficients, see page 37 of Rutten (2003). We use the definition of Wijbenga & Zwaan (1972) which normalizes b by the element abundance instead of the next-ion density.

between Stark and Van der Waals broadening in setting the broad wings of the Ca and Mg lines. The damping constant of the Mg line is about 1.7 times that of the Na line across the FALC photosphere and much larger in the Stark domain below $h = 0$ Mm.

We conclude from our FALC modeling:

- the Mg line has much larger opacity and somewhat larger damping than the Na line in the lower photosphere, hence its more prominent damping wings in Fig. 10 and its twice-larger equivalent width;
- its Boltzmann sensitivity to the declining temperature across the photosphere reduces the Mg line opacity to that of the Na line, so that they have nearly identical $\tau = 1$ heights in FALC;
- although the FALC chromosphere is not a realistic model of the actual chromosphere, this higher-layer opacity equality suggests that chromospheric fibrils can have similar opaqueness in the Mg and Na lines, as observed in Fig. 1;
- the various contributions to the κ variations around $h = 65$ km in Fig. 13 with their different temperature and density sensitivities produce the contrast differences along the first and last rows of Fig. 6. For example, the Ca line has lower contrast because it is not sensitive to ionization while its Boltzmann excitation causes contrast reduction (cf. Fig. 7 of Leenaarts et al. 2006b). The Mg and Na lines gain contrast from the κ sensitivities to ionization that produce dips at this height in Fig. 13;
- the Mg-line opacity has larger temperature sensitivity than the Na-line opacity due to its excitation energy. This may contribute to the larger clapotisphere transparency for Mg that is seen in the center row of Fig. 5;
- the Ca line has much larger opacity across all of FALC, which explains that it also maps chromospheric fibrils better than the other two lines. In the upper photosphere the Ca wings sample identical scenes as the other two lines but further out from line center, as seen in Figs. 5, 6;
- difference in resonance scattering explains that the Na line-center image in Fig. 4 appears the fuzziest, the Ca line-center image the sharpest. Similar sharpness difference is seen between the line-center Dopplergrams in Fig. 7, also for the simulation.

5.3. Granulation and reversed granulation

Comparison of the second and next-to-last rows in Figs. 4–6 confirms the imaging asymmetries in Fig. 1. Figure 10 shows that it does not have to do with mean-profile asymmetry. Figure 13 demonstrates that the Na line and Mg line have near-equal FALC core formation. Therefore, the reason for the imaging asymmetry must be dynamics that is not included in the FALC modeling. The Dopplergrams in Fig. 7 demonstrate that the reversed-granulation scenes in Figs. 4–6 are fully set by granular dynamics. The latter causes the imaging asymmetries.

Figure 14 is a simple demonstration for the Na line following the cartoon for Ba II 4554 Å in Fig. 6 of Sütterlin et al. (2001) with actual data. (Similar cartoons were already shown in Fig. 4 of Evans 1964.) The lane pixel has a redshifted profile that is darker than the mean profile, especially in the outer wings. The granule pixel has a profile close to the spatial mean but slightly blueshifted and slightly brighter in the outer wings. A filtergram near $\Delta\lambda = -14$ km s^{-1} as the first Na panel in Figs. 4–6 shows "flattened" granulation with smaller contrast than between nonshifted profiles. The reverse holds for the opposite sampling at $\Delta\lambda = +14$ km s^{-1}. This explains that in Figs. 4–6

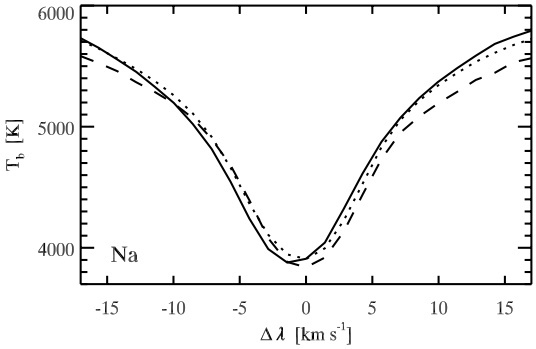

Fig. 14. Representative observed Na-line profiles to illustrate the cause of imaging asymmetries in granulation and reversed granulation. Solid: pixel at the center of a granule. Dashed: pixel in an intergranular lane. Dotted: spatial average.

the top Na panel shows lower granulation contrast than the bottom Na panel. The corresponding Dopplershift panels in Fig. 7 show the granulation even clearer, both for the observation and the simulation.

The same comparison for the Ca line shows no such difference, the corresponding observed Dopplergram only noise. The reason is simply that the comparable scene (or height) sampling takes place much further out in the extended damping wings of the Ca line, where these have a shallow slope so that profile shift has less effect. This is also the case for the Mg line which differs from the Na line in possessing extended wings (Fig. 10).

Let us now make such comparisons closer to the core. The blue wings of the lane and granule profiles in Fig. 14 cross, giving granulation contrast reversal which does not occur on the red side. These two pixels show reversed granulation with reversed imaging asymmetry. The effect is again larger for steeper line flanks. The corresponding sampling temperature of about 5000 K lies above the onset of the Mg and Ca wings in Fig. 12. Therefore, the striking imaging asymmetry between the wings of the Na line in Fig. 1 is also simply due to their steepness (Fig. 10). The same asymmetry should appear in the inner core of other narrow but somewhat weaker lines; indeed it is very pronounced for Fe I 7090.4 Å in Fig. 5 of Janssen & Cauzzi (2006).

The diffuse-gray lane patterns in the middle-row Dopplergrams in Fig. 7 correspond well to the vertical velocity pattern at $z = 0.3$ Mm in the last row of Fig. 5 of Leenaarts et al. (2010) and qualitatively to the similar pattern at $\tau = 0.1$ in Fig. 3 of Cheung et al. (2007). Such simulations also show slight temperature contrast reversal between granules and lanes at such heights, in our case illustrated for $z = 0.3$ Mm in the second row of Fig. 5 of Leenaarts et al. (2010). It was already explained by Nordlund (1984b) on pages 15–18 in his informative analysis of his pioneering granulation simulation as due to radiative reheating along bend-over flow trajectories, as those in Fig. 6 of Cheung et al. (2007). The Dopplershift-brightening pattern combination produces slender near-lane brightness features as seen in the second row of Fig. 4. They correlate only roughly with underlying intergranular lanes, best at a delay of 1–2 min. In addition, at larger height gravity wave interference takes over from direct granular overshoot and reduces the correspondence (cf. Rutten et al. 2004; Leenaarts & Wedemeyer-Böhm 2005; Janssen & Cauzzi 2006; Straus et al. 2008).

The conclusion from this section is that the imaging asymmetries between the Na wings and between the Mg and Na lines in Fig. 1 arise from the correlated brightness and Dopplershift patterns in the solar granulation and its overshoot, to which the

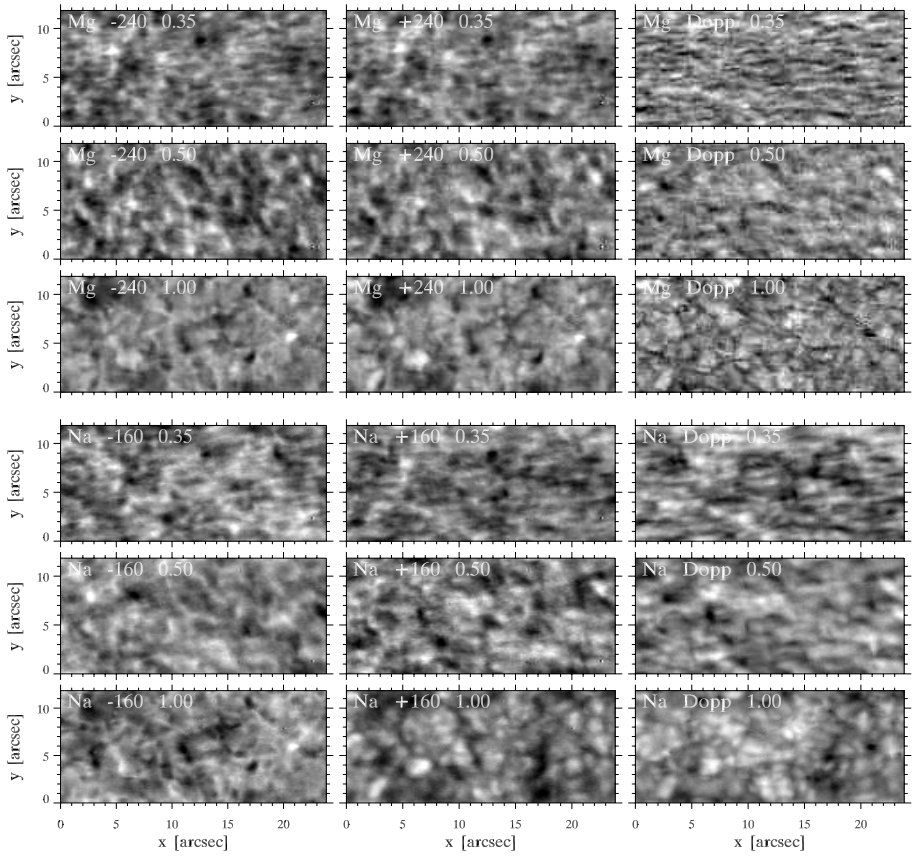

Fig. 15. Comparable intensity images from Hinode in the Mg line (*upper half*) and Na line (*lower half*). Each panel is independently grayscaled for optimum contrast. The subfield has the same size as in Figs. 4–7. Along rows the images cover the same scene, with about 32 s delay between the two lines. The viewing angle differs between rows, with $\mu = 0.35$, 0.50 and 1.00 as specified. The limb is to the top. The first two columns are images in the blue and red wing at $\Delta\lambda = \pm 240$ mÅ for the Mg line, $\Delta\lambda = \pm 160$ mÅ for the Mg line. The third column has the corresponding $(I_{\rm red} - I_{\rm blue})/(I_{\rm red} + I_{\rm blue})$ Dopplergrams.

Na line is more sensitive because it does not have strong damping wings.

5.4. Line core scenes

All three lines are scattering lines, the Na line the worst. Their core intensities are set by radiation escape in deeper layers than the last scatterings. The latter set the Dopplershift encoding (assuming complete redistribution which is in order even for the Na line, see Uitenbroek & Bruls 1992). This sampling difference is most clearly demonstrated by the simulated Mg core, which shows regular granulation much clearer in intensity than in its Dopplergram. The difference also explains that the large image variations between the three central rows of Figs. 4–6 are largely produced by the Dopplershifts in the bottom rows of Fig. 7. Therefore, taking Dopplergrams represents a much better use of these lines than taking intensity filtergrams.

The rough correspondence of the bright and dark Mg and Na Dopplergram patches in the third row of Fig. 7 with the areas of brighter and less bright granules in the first row suggests that these are *p*-mode oscillation patches that result from global interference patterning, with larger D in the blueshifted phase. The lambdameter phase difference measurements for Na I D_2 of Deubner et al. (1996) indeed show oscillation coherence between the outer wing and core, but only for the five-minute component (last panel of their Fig. 6). For increasing height the oscillation dominance shifts from five-minute evanescent global mode interference to more local three-minute propagating waves, as seen already in the somewhat deeper layers sampled by ultraviolet continua (e.g., Krijger et al. 2001), and then to three-minute shocks that are seen in the Ca line (next section). The lack of coherence at higher frequency in Fig. 6 of Deubner et al. (1996) suggests that the Mg and Na core Dopplergrams already have some sensitivity to these shocks.

The simulation does not contain global *p*-mode oscillation interference patterning but has its own box modes and generates its own propagating waves. The fine structure across the last row of Fig. 7 shows that all three lines Doppler-sense the very inhomogeneous shock-ridden clapotisphere that results, even though it appears too transparent in the simulated Mg line (Sect. 7). We refer to Leenaarts et al. (2009, 2010) for pertinent displays. In particular, Fig. 9 of the latter paper contains informative formation breakdown diagrams for the Na and Ca lines. Comparing these to Fig. 13 demonstrates enormous line formation variations with respect to FALC modeling.

The conclusion of this section is that the line cores primarily sample wave patterns that likely include shock interference.

5.5. Magnetic concentrations and shocks

There are only a few magnetic concentrations in the observed subfield, more in the simulation. In Figs. 4–6 they stand out as bright features in the outer line wings, often brighter than the brightest granules because lack of collisional damping in the partially evacuated concentrations reduces the wing opacity (cf. Leenaarts et al. 2006a,b).

Nearer the line centers they no longer stand out as bright points but rather as profile asymmetry features, producing small, roundish, dark features in the Mg and Na Dopplergrams in Fig. 7. Figure 8 uses the V/R asymmetry ratio following the example for Ca II H_{2V} grains of Cram & Damé (1983). The formation diagrams of such grains in Carlsson & Stein (1997) show that H_{2V} grain asymmetry results from line-of-sight integration through cool postshock downflows around $h = 1.5$ Mm and grain-producing upcoming hot fresh shocks around $h = 1$ Mm.

The same pattern occurs for rarefied magnetic concentrations at heights of only a few hundred kilometers, where the outside scene is still reversed granulation. The ubiquity of photospheric shocks in and near isolated magnetic concentrations was first suggested by Steiner et al. (1998). Their signature in the Na core was also noted by Jess et al. (2010).

A detailed demonstration is given by the Na-line formation diagrams in the first quartet of Fig. 7 of Leenaarts et al. (2010), which analyze the magnetic concentration at $(x, y) = (8.2, 7.2)$ in the simulation snapshot. It has a shock at $z \approx 0.3$ Mm that produces an emission peak just blue of Na line center, in the same manner as a H_{2V} grain but much deeper. The post-shock downdrafts from shocks that previously passed, now at $z \approx 0.5$ and 1.0 Mm, produce a red-shifted line core which is very dark because the strongly scattering Na source function decouples from the Planck function already at $h \approx 0.2$ Mm and shows no sensitivity to the actual high-temperature plateau over $h \approx 0.3$–0.7 Mm. Such raised temperature plateaus in magnetic concentrations are attributed to Joule heating by Carlsson et al. (2010). They are similar to the FALC chromospheric temperature plateau but occur at photospheric heights.

Note that when such a spectral emission peak blueshifts into an inner-wing sampling passband, the Dopplergram sign of $D \equiv (T_b^{red} - T_b^{blue})/(T_b^{red} + T_b^{blue})$ becomes the same as for a redshifted absorption core. K_{2V}-like grains can therefore appear black in our D definition. Similarly, the asymmetry ratio V/R of Fig. 8 may exceed unity both due to fresh-shock bright updraft and to dark post-shock downfall, i.e., for both phases of shock modulation and especially when these combine along the line of sight.

The Ca image just blue of line center in the third row of Fig. 4 does show non-magnetic bright grains that represent the Ca-line analog to higher-formed internetwork K_{2V} grains. Their visibility is to be expected from the similar core asymmetries in all five Ca II lines in Fig. 11. They are indeed black in the corresponding Dopplergram in Fig. 7. The center-row Ca diagram in Fig. 8 suggests larger spatial filling factor for these shocks. The simulation diagram even has a secondary contour peak for them.

Outside magnetic concentrations the Na and Mg lines are too weak to produce internetwork grains. Nevertheless, the Na-core V/R distribution tail in the central diagram of Fig. 8 suggests that the Na line senses internetwork shocks similarly to the Ca line.

The conclusion of this section is that Na and Mg core Dopplergrams or asymmetry images turn out to be quasi-magnetograms by mapping photospheric shocks in or near strong-field concentrations. Outside these, only the Ca line shows mean-profile asymmetry from clapotispheric internetwork shocks.

6. Center-to-limb variation

Figure 15 presents a selection from the Hinode observations, added to show how limbward viewing affects the three lines. The $\Delta\lambda$ values are selected for scene similarity at $\mu = 1$. These images (bottom rows of each half) have lower quality than the SST/CRISP images but again show similar imaging asymmetry as in Fig. 1: similar reversed granulation in the blue Mg and Na wings and the red Mg wing, granular-like patterning instead in the red Na wing. The $\mu = 1$ Dopplergrams also show granulation, with larger contrast in the Na line.

At $\mu = 0.5$ the pattern repeats but with less discrepancy for the Na red wing, less difference between the Dopplergrams, and general foreshortening. The decrease in imaging asymmetry corresponds to smaller Dopplershifts from the vertical motions.

Closer to the limb a different pattern of horizontal stripings appears, similarly in all $\mu = 0.35$ panels and clearest in the Mg Dopplergram. It looks rather like the supergranulation in the discovery plate in Fig. 6 of Leighton et al. (1962) but of course the scale is much smaller: these are horizontal outflows in granulation cells rather than in supergranulation cells. At this formation height they probably correspond to the bend-over flow lines of Cheung et al. (2007). In the Na Dopplergram some dark patches are visible which are likely clapotispheric clouds that are not visible in the Mg line due to lack of Boltzmann excitation.

7. Discussion

In Figs. 4–7 we chose to jump from deep outer-wing formation ($h \approx 150$ km) in the second rows to line-core formation in the next rows to avoid figure clutter and to skip observation-simulation sampling differences set by the too narrow simulated Ca and Mg cores. In the observations the intervening scenes, best seen per Dopplergram, are simply the combination of the (reversed) granulation and overlying larger-scale oscillation patches. The cloud-like appearance of the latter suggests bimodal formation, with the deeper layers well described by Eddington-Barbier sampling near $\tau = 1$, the upper layers better described by Schuster-Schwarschild clouds with Dopplershift as the most important cloud parameter. The inner-core panels in Fig. 6 of Deubner et al. (1996) confirm the notion of cloud-like common Dopplershift at all frequencies. In the simulation the visibility of a gray low-Dopplershift intermediate background scene that appears especially in the outer Ca core is likely due to incomplete masking by clapotispheric clouds that are too transparent.

Cauzzi et al. (2009, 2008) suggested such bimodal formation for chromospheric fibrils in the Ca line. These indeed blanket the inner Ca core even more when there is more activity than in the very quiet area analysed here. In the Balmer lines they even tend to obscure the reversed granulation (Leenaarts et al. 2006b). Note that Evans & Catalano (1972) already reported not finding negative "oddities" for Hβ (but note also that Thomas 1972, as referee blamed fibril source functions, not opacities).

The simulation snapshot and line synthesis do a good job in reproducing and so helping to explain the imaging asymmetry between the Na line and the other two lines, but they do not reproduce the observations in the line cores very well. These are not the main topic here so we discuss these discrepancies only briefly, again referring to Leenaarts et al. (2009, 2010) for more detail. The major ones are the larger visibility of granulation at the center of the Mg line, the narrower core width of the Ca line in the simulation, and the differences in core asymmetry sampling in Fig. 8.

The clapotispheric cool-cloud transparency in the simulated Mg line is likely an artifact due to underestimation of the Mg I density, for the same reason as the underestimation of the Na I density in these cool clouds discussed in Leenaarts et al. (2010): since in the simulation the ionization equilibria are assumed to be in LTE, the electron-donor elements (Si, Fe, Al, Mg) are less ionized than they would be if the actual domination by photoionization was properly accounted for. The resulting underestimation of the electron density is 1–2 orders of magnitude, higher up even 3–4 if one compares with time-dependent hydrogen ionization balancing in cool post-shock gas (Leenaarts et al. 2007). In contrast, the synthesis codes implement photoionization properly, so these yield higher ionization rates, but the recombination lacks electrons so that the balance shifts to the ion state and the line opacity is severely underestimated. Thus, the

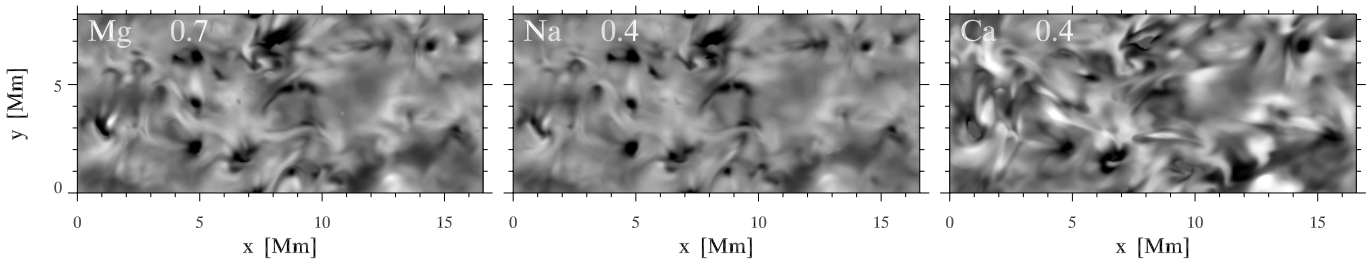

Fig. 16. Dopplergrams from the simulation as in the bottom row of Fig. 7 but closer to line center and with only CRISP spectral smearing, no spatial PSF smearing.

cool clouds are too transparent in the simulated Na and Mg lines, more so in the latter due to its 2.7 eV excitation energy. Possibly the Ca line is similarly affected higher up in cool clouds by similarly overestimated ionization from Ca II to Ca III. Such transparencies may contribute to the differences in Fig. 8.

The too narrow core width of the Ca line was noted and discussed by Leenaarts et al. (2009). The apparent need for "microturbulent broadening" in higher layers suggests a lack of numerical resolution, just as the solar granulation needed microturbulent fudging until simulation resolution did away with that (Nordlund 1980, 1984b). Indeed, a test with the higher-resolution simulation of Carlsson et al. (2010) shows larger broadening. The assumption of instantaneous LTE ionization balancing not only causes underestimation of the electron densities in cool clouds and corresponding underestimation of the opacities of our three lines, but also of the clapotispheric dynamics (Leenaarts et al. 2007).

These deficiencies suggest that the actual clapotispheric contributions to these line cores may be even more wildly structured than Figs. 6, 7 suggest already. Figure 16 displays innermost-core Dopplergrams from the simulation after only spectral smearing with the CRISP transmission functions. The spectral smearing affects the core depth considerably (Fig. 9) but the Dopplergram scene keeps its structure. The scene is a violent one with sharp bright fronts, dark cool clouds, and black magnetic concentrations. Comparison of Fig. 16 to the Na line-center Dopplershift panel in Fig. 7 of Leenaarts et al. (2010) shows that the CRISP-smeared Dopplergram gives a good rendering of the actual Dopplershifts, with more emphasis on magnetic concentrations. Comparison of Fig. 16 to the center rows of Fig. 5 shows that the simulated line cores are so much dominated by Doppler modulation that inner-core Doppler measurement is mandatory in using these lines as upper-atmosphere diagnostics. Comparison of Fig. 16 to the line-core rows of Fig. 7 suggests that higher spatial resolution than in our observations is highly desirable.

A corollary is that searches for global g-modes and so-called "chromosphere seismology" using full-disk resonance-cell sampling of the Na line as with GOLF-NG (e.g., Turck-Chièze et al. 2006; Salabert et al. 2009) will suffer noise from reversed granulation just as classical helioseismology suffers noise from granulation. Magnetic concentrations contribute much noise (literally) by their shocks. GOLF-NG's 15 passbands, spread over $\Delta\lambda = \pm 9$ km s^{-1}, have $FWHM = 30$ mÅ, half CRISP's passband in this line and clearly narrow enough. Interpretation of such multi-passband oscillation sampling that relies on one-dimensional height-of-formation interpretation, for example to diagnose upward propagation from inward phase difference, is likely to fail since the clapotispheric signals are better described as clouds of varying opacity at varying height of which the varying Dopplershifts act as shutters obscuring the inner line wings.

8. Conclusion

There is a striking imaging asymmetry between Na I D_1 and Mg I b_2 in Fig. 1: the Mg line shows reversed granulation in both wings, but the Na line shows similar reversed granulation only in its blue wing, normal granulation in its red wing. This is due to different sensitivity to the correlated Dopplershift and brightness pattern of the reversed granulation in the mid-photosphere. The Mg line has larger opacity and damping in deeper layers, hence wider damping wings, hence less steep profile flanks, hence smaller Doppler sensitivity. Both lines sample the same layers in both their wings; only the appearance of the granulation and the reversed granulation differ between these, not their physical nature or sampling height.

The cores of the Mg and Na lines are formed remarkably similarly. Dopplergrams in these represent their primary diagnostic value and can also serve to detect and study magnetic concentrations marked by photospheric shocks.

Center-to-limb observations with at least the quality of the disk-center SST/CRISP data used here will be well-suited to constrain the reversed-granulation domain further and to enlarge the testing ground for numerical simulations.

When the lack of line-core opacity and broadening in the simulation is resolved, the obvious next step is to compare time sequences of such imaging spectroscopy and simulations for these lines in Fourier analyses as those of e.g., Fleck & Deubner (1989) and Deubner et al. (1996).

The small structural scales that are predicted by the simulations to dominate at clapotispheric heights define the need for high spatial resolution, considerably higher even than reached here, as a principal quest in probing this domain of the solar atmosphere.

Acknowledgements. We thank T. D. Tarbell and P. Sütterlin for the discussions that inspired this paper and T. Leifsen, H. Skogsrud and A. Ortiz for obtaining the CRISP scan in Fig. 1 that initiated these discussions. The SST is operated by The Institute for Solar Physics of the Royal Swedish Academy of Sciences at the Spanish Observatorio del Roque de los Muchachos of the Instituto de Astrofísica de Canarias. The Japanese Hinode mission was developed and launched by ISAS/JAXA, with NAOJ as domestic partner and NASA and STFC as international partners, and is operated by these agencies in co-operation with ESA and NSC. R.J.R.'s travel to the SST and to Oslo was funded by the EC through the SOLAIRE Network (MTRN-CT-2006-035484). Discussions at NAOJ (Mitaka, Japan) while R.J.R. was a visitor there also contributed to this paper, and he completed it as a visitor at LMSAL (Palo Alto, USA). As always, our work was much facilitated by NASA's ADS.

References

Altrock, R. C., & Musman, S. 1976, ApJ, 203, 533
Avrett, E. H. 1985, in Chromospheric Diagnostics and Modelling, ed. B. W. Lites, 67
Bard, S., & Carlsson, M. 2008, ApJ, 682, 1376
Botnen, A. 1997, Master's thesis, Inst. Theor. Astrophys. Oslo
Bruls, J. H. M. J., Rutten, R. J., & Shchukina, N. G. 1992, A&A, 265, 237
Canfield, R. C., & Mehltretter, J. P. 1973, Sol. Phys., 33, 33

Carlsson, M. 1986, Uppsala Astron. Obs. Reports, 33
Carlsson, M., & Stein, R. F. 1994, in Chromospheric Dynamics, ed. M. Carlsson, 47
Carlsson, M., & Stein, R. F. 1997, ApJ, 481, 500
Carlsson, M., Rutten, R. J., & Shchukina, N. G. 1992, A&A, 253, 567
Carlsson, M., Hansteen, V. H., & Gudiksen, B. V. 2010, MemSAI, 81, 582
Cauzzi, G., Reardon, K. P., Uitenbroek, H., et al. 2008, A&A, 480, 515
Cauzzi, G., Reardon, K., Rutten, R. J., Tritschler, A., & Uitenbroek, H. 2009, A&A, 503, 577
Cheung, M. C. M., Schüssler, M., & Moreno-Insertis, F. 2007, A&A, 461, 1163
Collados, M., & Vázquez, M. 1987, A&A, 180, 223
Collet, R., Asplund, M., & Thévenin, F. 2005, A&A, 442, 643
Cram, L. E., & Damé, L. 1983, ApJ, 272, 355
De Pontieu, B., Hansteen, V. H., Rouppe van der Voort, L., van Noort, M., & Carlsson, M. 2007, ApJ, 655, 624
Deubner, F. L., & Mattig, W. 1975, A&A, 45, 167
Deubner, F., Waldschik, T., & Steffens, S. 1996, A&A, 307, 936
Evans, J. W. 1964, Astrophys. Norveg., 9, 33
Evans, J. W., & Catalano, C. P. 1972, Sol. Phys., 27, 299
Fleck, B., & Deubner, F. 1989, A&A, 224, 245
Fleck, B., Straus, T., Carlsson, M., et al. 2010, MemSAI, 81, 777
Fontenla, J. M., Avrett, E. H., & Loeser, R. 1993, ApJ, 406, 319
Fontenla, J. M., Curdt, W., Haberreiter, M., Harder, J., & Tian, H. 2009, ApJ, 707, 482
Hansteen, V. H., De Pontieu, B., Rouppe van der Voort, L., van Noort, M., & Carlsson, M. 2006, ApJ, 647, L73
Hansteen, V. H., Carlsson, M., & Gudiksen, B. 2007, in The Physics of Chromospheric Plasmas, ed. P. Heinzel, I. Dorotovič, & R. J. Rutten, ASP Conf. Ser., 368, 107
Janssen, K., & Cauzzi, G. 2006, A&A, 450, 365
Jess, D. B., Mathioudakis, M., Christian, D. J., Crockett, P. J., & Keenan, F. P. 2010, ApJ, 719, L134
Kosugi, T., Matsuzaki, K., Sakao, T., et al. 2007, Sol. Phys., 243, 3
Krijger, J. M., Rutten, R. J., Lites, B. W., et al. 2001, A&A, 379, 1052
Leenaarts, J., & Carlsson, M. 2009, in The Second Hinode Science Meeting: Beyond Discovery-Toward Understanding, ed. B. Lites, M. Cheung, T. Magara, J. Mariska, & K. Reeves, ASP Conf. Ser., 415, 87
Leenaarts, J., & Wedemeyer-Böhm, S. 2005, A&A, 431, 687
Leenaarts, J., Rutten, R. J., Carlsson, M., & Uitenbroek, H. 2006a, A&A, 452, L15
Leenaarts, J., Rutten, R. J., Sütterlin, P., Carlsson, M., & Uitenbroek, H. 2006b, A&A, 449, 1209
Leenaarts, J., Carlsson, M., Hansteen, V., & Rutten, R. J. 2007, A&A, 473, 625
Leenaarts, J., Carlsson, M., Hansteen, V., & Rouppe van der Voort, L. 2009, ApJ, 694, L128
Leenaarts, J., Rutten, R. J., Reardon, K., Carlsson, M., & Hansteen, V. 2010, ApJ, 709, 1362
Leighton, R. B., Noyes, R. W., & Simon, G. W. 1962, ApJ, 135, 474
Levy, M. 1971, A&A, 14, 15
Lockyer, N. 1868, Procs. Royal Soc. London, 17, 131
Maltby, P., Avrett, E. H., Carlsson, M., et al. 1986, ApJ, 306, 284
Moore, C. E., Minnaert, M. G. J., & Houtgast, J. 1966, The solar spectrum 2935 Å to 8770 Å
Neckel, H. 1999, Sol. Phys., 184, 421
Neckel, H., & Labs, D. 1984, Sol. Phys., 90, 205
Nordlund, A. 1980, Stellar Turbulence, ed. D. F. Gray, & J. L. Linsky, IAU Colloq., 51. Lecture Notes in Physics (Springer), 114, 213
Nordlund, A. 1984a, in Small-Scale Dynamical Processes in Quiet Stellar Atmospheres, ed. S. L. Keil, 174
Nordlund, A. 1984b, in Small-Scale Dynamical Processes in Quiet Stellar Atmospheres, ed. S. L. Keil, 181
Owocki, S. P., & Auer, L. H. 1980, ApJ, 241, 448
Roddier, F. 1981, Prog. Opt., 19, 281
Rouppe van der Voort, L., Leenaarts, J., De Pontieu, B., Carlsson, M., & Vissers, G. 2009, ApJ, 705, 272
Rutten, R. J. 1988, in Physics of Formation of FE II Lines Outside LTE, ed. R. Viotti, A. Vittone, & M. Friedjung, IAU Colloq., 94, ASSL (Springer), 138, 185
Rutten, R. J. 1995, in Helioseismology, ESA SP, 376, 151
Rutten, R. J. 2003, Radiative Transfer in Stellar Atmospheres, Lecture Notes Utrecht University
Rutten, R. J. 2010, MemSAI, 81, 565
Rutten, R. J., & Uitenbroek, H. 1991, Sol. Phys., 134, 15
Rutten, R. J., De Wijn, A. G., & Sütterlin, P. 2004, A&A, 416, 333
Salabert, D., Turck-Chièze, S., Barrière, J. C., et al. 2009, in Solar-Stellar Dynamos as Revealed by Helio- and Asteroseismology: GONG 2008/SOHO 21, ed. M. Dikpati, T. Arentoft, I. González Hernández, C. Lindsey, & F. Hill, ASP Conf. Ser., 416, 341
Scharmer, G. B., Bjelksjo, K., Korhonen, T. K., Lindberg, B., & Petterson, B. 2003a, SPIE Conf. Ser., 4853, 341
Scharmer, G. B., Dettori, P. M., Löfdahl, M. G., & Shand, M. 2003b, SPIE Conf. Ser., 4853, 370
Scharmer, G. B., Narayan, G., Hillberg, T., et al. 2008, ApJ, 689, L69
Schüssler, M., Shelyag, S., Berdyugina, S., Vögler, A., & Solanki, S. K. 2003, ApJ, 597, L173
Shelyag, S., Schüssler, M., Solanki, S. K., Berdyugina, S. V., & Vögler, A. 2004, A&A, 427, 335
Steiner, O., Grossmann-Doerth, U., Knölker, M., & Schüssler, M. 1998, ApJ, 495, 468
Straus, T., Fleck, B., Jefferies, S. M., et al. 2008, ApJ, 681, L125
Suematsu, Y., Tsuneta, S., Ichimoto, K., et al. 2008, Sol. Phys., 249, 197
Suemoto, Z., Hiei, E., & Nakagomi, Y. 1987, Sol. Phys., 112, 59
Suemoto, Z., Hiei, E., & Nakagomi, Y. 1990, Sol. Phys., 127, 11
Sütterlin, P., Rutten, R. J., & Skomorovsky, V. I. 2001, A&A, 378, 251
Thomas, R. N. 1972, Sol. Phys., 27, 303
Tsuneta, S., Ichimoto, K., Katsukawa, Y., et al. 2008, Sol. Phys., 249, 167
Turck-Chièze, S., Carton, P., Ballot, J., et al. 2006, Adv. Space Res., 38, 1812
Uitenbroek, H. 1989, A&A, 213, 360
Uitenbroek, H., & Bruls, J. H. M. J. 1992, A&A, 265, 268
van Noort, M., Rouppe van der Voort, L., & Löfdahl, M. G. 2005, Sol. Phys., 228, 191
van Noort, M. J., & Rouppe van der Voort, L. H. M. 2008, A&A, 489, 429
Vernazza, J. E., Avrett, E. H., & Loeser, R. 1981, ApJS, 45, 635
Wedemeyer-Böhm, S. 2008, A&A, 487, 399
Wedemeyer-Böhm, S., & Rouppe van der Voort, L. 2009, A&A, 503, 225
Wijbenga, J. W., & Zwaan, C. 1972, Sol. Phys., 23, 265